ACS APPLIED MATERIALS & INTERFACES

www.acsami.org

Research Article

Tumor-Penetrable Nitric Oxide-Releasing Nanoparticles Potentiate Local Antimelanoma Therapy

Juho Lee, Shwe Phyu Hlaing, Nurhasni Hasan, Dongmin Kwak, Hyunwoo Kim, Jiafu Cao, In-Soo Yoon, Hwayoung Yun, Yunjin Jung, and Jin-Wook Yoo*

Cite This: *ACS Appl. Mater. Interfaces* 2021, 13, 30383–30396

Read Online

ACCESS | Metrics & More | Article Recommendations | Supporting Information

ABSTRACT: Although nitric oxide (NO) has been emerging as a novel local anticancer agent because of its potent cytotoxic effects and lack of off-target side effects, its clinical applications remain a challenge because of the short effective diffusion distance of NO that limits its anticancer activity. In this study, we synthesized albumin-coated poly(lactic-*co*-glycolic acid) (PLGA)-conjugated linear polyethylenimine diazeniumdiolate (LP/NO) nanoparticles (Alb-PLP/NO NPs) that possess tumor-penetrating and NO-releasing properties for an effective local treatment of melanoma. Sufficient NO-loading and prolonged NO-releasing characteristics of Alb-PLP/NO NPs were acquired through PLGA-conjugated LP/NO copolymer (PLP/NO) synthesis, followed by nanoparticle fabrication. In addition, tumor penetration ability was rendered by the electrostatic adsorption of the albumin on the surface of the nanoparticles. The Alb-PLP/NO NPs showed enhanced intracellular NO delivery efficiency and cytotoxicity to B16F10 murine melanoma cells. In B16F10-tumor-bearing mice, the Alb-PLP/NO NPs showed improved extracellular matrix penetration and spatial distribution in the tumor tissue after intratumoral injection, resulting in enhanced antitumor activity. Taken together, the results suggest that Alb-PLP/NO NPs represent a promising new modality for the local treatment of melanoma.

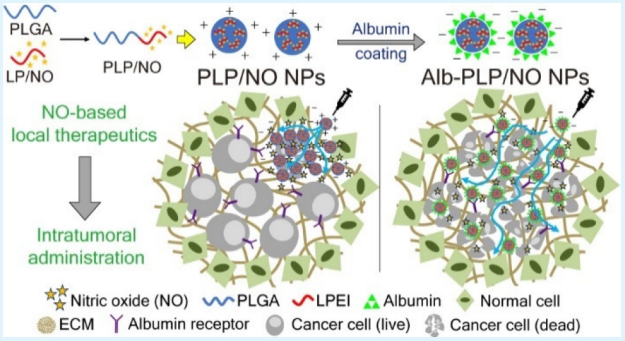

KEYWORDS: *nitric oxide, nitric oxide releasing nanoparticles, melanoma, local anticancer therapy, tumor penetration, intratumoral injection*

Downloaded via BHARATHIAR UNIV on August 11, 2021 at 03:37:45 (UTC).
See https://pubs.acs.org/sharingguidelines for options on how to legitimately share published articles.

1. INTRODUCTION

Melanoma is the fifth most common cancer in the United States and the most aggressive form of skin cancer.[1] It accounts for >80% of deaths from skin cancer worldwide, but its incidence and resulting mortality are increasing.[2−4] Currently, the development of nonsurgical local therapeutics, including topical and intratumoral-injectable formulations containing chemotherapeutic agents, has garnered interest to treat melanoma patients who are not good surgical candidates or those who are concerned about scarring in cosmetically sensitive areas.[5−7] Nevertheless, local melanoma treatment with chemotherapeutic agents has achieved only limited success due to the drug resistance of melanoma to various anticancer agents and the potential risk of off-target toxicity to normal tissues such as ulceration, erythema, edema, epidermolysis, and deep tissue damage, which cause severe functional disturbance of the skin.[8−13] Therefore, it is integral to develop effective intratumoral-injectable anticancer therapeutics that could potentiate the cytotoxic effects on melanoma cells without off-target side effects to take full advantages of local treatment of melanoma.

In recent years, nitric oxide (NO), an endogenous gaseous molecule, has emerged as a promising anticancer agent that not only exerts potent cytotoxic effects against various cancer cells but also minimizes off-target side effects due to its rapid transformation to harmless products after its pharmacological generation.[14−16] NO promotes cancer progression at low concentrations (<30 nM) and exerts potent cytotoxic effects at high concentrations (>400 nM).[17] When cancer cells are exposed to high levels of NO, they can suffer DNA damage as well as disruptions in energy metabolism and mitochondrial function.[18] Moreover, NO can induce cell death via p53 phosphorylation (at >400 nM) and nitrosative stress (at >1 μM).[19,20] Other mechanisms of NO activity have also been reported, including apoptosis by p53 upregulation,[21] anti-apoptotic molecule degradation,[22] and cytochrome *c* release,[23]

Received: April 22, 2021
Accepted: June 15, 2021
Published: June 24, 2021

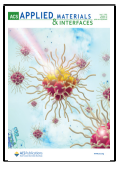

© 2021 American Chemical Society

https://doi.org/10.1021/acsami.1c07407
ACS Appl. Mater. Interfaces 2021, 13, 30383−30396

as well as cell cycle arrest and cell necrosis by peroxynitrile formation.[24,25] Thus, by exposing cancer cells to high concentrations of NO, potent anticancer effects could be achieved in treating melanoma.

Despite the potent antitumor activity of NO, however, its clinical application for the local treatment of melanoma remains challenging due to its gaseous and short-lived nature.[26] Since NO exerts cytotoxic effects inside cancer cells, a sufficient amount of NO needs to be delivered intracellularly to achieve successful anticancer effects.[27,28] This reason has propelled the development of NO-releasing nanoparticles that increase NO concentrations inside cancer cells due to cellular internalization and controlled NO release.[29] During the past decade, several studies have demonstrated that NO-releasing nanoparticles exhibit potent *in vitro* cytotoxicity against cancer cells in 2D cell culture models.[29−31] However, to the best of our knowledge, the successful anticancer activity of NO-releasing nanoparticles in animal models has yet to be reported, presumably because of the complex structure of tumor tissue along with the unique properties of NO. Unlike 2D cell culture models, tumor tissues are a three-dimensional structure containing cancer cells along with other components, such as stromal cells, macrophages, and dense extracellular matrix (ECM).[32,33] In particular, ECM comprises up to 60% of the whole tumor mass;[34] hence, it is essential to evaluate ECM penetration to develop effective NO-based local therapeutics for melanoma. Moreover, NO is a very short-lived molecule (half-life of only a few seconds) and has a limited diffusion distance of only 40−200 μm under physiological conditions.[35−37] Thus, effective anticancer activity against melanoma can only be achieved when the NO delivery system penetrates the entire melanoma tissue and releases NO in a controlled manner to provide sufficient amounts of NO (>400 nM to exert cytotoxic effects)[17] to the cancer cells. Otherwise, a limited anticancer effect would only be achieved near the injection site due to the short half-life and limited diffusion distance of NO.

Herein, we report the synthesis and testing of novel albumin-coated NO-releasing nanoparticles that penetrate melanoma tissue and generate prolonged release of sufficient NO for effective local melanoma therapy. Hydrophobic poly(D,L-lactic-*co*-glycolic acid) (PLGA) was covalently conjugated to hydrophilic low molecular weight linear polyethylenimine diazeniumdiolate (LP/NO), which is a widely used NO donor.[38−41] Linear polyethylenimine (LPEI) contains abundant secondary amine groups that can immobilize diazeniumdiolates.[38] In addition, LPEI has been successfully introduced into phase I and II clinical studies for treating ovarian, pancreatic, and superficial bladder cancers with a good safety profile.[42−44] The nanoparticles were fabricated using PLGA-conjugated LP/NO copolymer (PLP/NO) followed by surface modification with bovine serum albumin (BSA). The surface modification with albumin alters the surface charge of the nanoparticles, thus facilitating tumor penetration by reducing their ECM interaction.[45] Albumin-coated nanoparticles could show enhanced cellular uptake since the overexpressed albumin receptors on cancer cells facilitate cellular uptake of albumin-coated nanoparticles.[46−48] After physicochemical characterization of the newly synthesized PLP/NO and albumin-coated PLP/NO nanoparticles (Alb-PLP/NO NPs), their cytotoxicity, cellular uptake, and ECM penetration were investigated using a series of *in vitro* experiments. Furthermore, the *in vivo* antitumor efficacy and spatial distribution of intratumorally administered Alb-PLP/NO NPs were evaluated using a B16F10 melanoma cell bearing C56BL/6 mouse model.

2. EXPERIMENTAL SECTION

2.1. Materials. Linear polyethylenimine (LPEI) (MW 2.5 kDa) was purchased from Polysciences, Inc. (Warrington, PA). PLGA (lactide/glycolide = 50/50, MW 30 kDa, acid end-cap) was purchased from PolySciTech (Akina, Inc., West Lafayette, IN). BSA was purchased from Santa Cruz Biotechnology (Dallas, TX). 11-Chloro-1,1′-di-*n*-propyl-3,3,3′,3′-tetramethyl-10,12-trimethyleneindatricarbocyanine iodide (IR780) was purchased from Alfa Aesar (Haverhill, MA). Poly(vinyl alcohol) (PVA), 2,2,2-tribromoethanol, *tert*-amyl alcohol, 4′,6-diamidino-2-phenylindole dihydrochloride (DAPI), chloroform-*d* ($CDCl_3$, 99.8 atom % D + 0.03 (v/v) % TMS), Nile red, and thiazolyl blue tetrazolium bromide (MTT) were purchased from Sigma-Aldrich (St. Louis, MO). Eosin Y solution was purchased from Daejung Chemicals & Metals Co., Ltd. (Shiheung, Korea). Hematoxylin solution, sodium methoxide, *N*-hydroxysulfosuccinimide (NHS), and trehalose were purchased from Wako Pure Chemical (Osaka, Japan). 1-Ethyl-3-(3-(dimethylamino)propyl)carbodiimide hydrochloride (EDC) was purchased from Dojindo Laboratories (Kumamoto, Japan). 3-Amino,4-aminomethyl-2′,7′-difluorescein diacetate (DAF-FM DA) and the Click-iT Plus TUNEL assay kit were purchased from Invitrogen (Camarillo, CA). Geltrex matrix was purchased from Gibco (Carlsbad, CA). Argon (Ar) and NO gases were purchased from HANA gas (Gimhae, Korea). All other reagents and solvents were of the highest analytical grade.

2.2. Polymer Synthesis. LP/NO was synthesized as described previously with some modifications.[49] Briefly, 2 g of LPEI and 1.3 g of sodium methoxide were dissolved in 200 mL of anhydrous methanol/tetrahydrofuran (THF) (1:1 v/v ratio). After the solution was placed in a high-pressure reactor, the chamber was purged with 10 psi of Ar for 5 min and charged with 80 psi of NO. Three days later, after Ar flushing, ice-cold diethyl ether was added to the solution to precipitate the LP/NO. After washing three times with diethyl ether, the LP/NO was vacuum-dried and stored at −20 °C for future use. To characterize the LP/NO, the distinctive absorption band of the diazeniumdiolate groups was measured on a UV/vis spectrophotometer (Optizen 2120 UV, Mecasys, Republic of Korea), and Fourier transform infrared (FT-IR) spectra were recorded on a Spectrum GX FT-IR spectrometer (PerkinElmer, Norwalk, CT) using the KBr pellet method.

PLP/NO was synthesized via carbodiimide-mediated esterification between the carboxyl end of PLGA and the hydroxyl end of LP/NO. Briefly, for PLGA activation, 1 g of PLGA, 65 mg of EDC, and 40 mg of NHS were dissolved in 20 mL of dichloromethane (DCM) at 30 °C for 12 h. After incubation, the PLGA-NHS was collected by precipitation using excess methanol. The residual EDC and NHS were removed by washing twice with methanol. The PLGA-NHS was dried under vacuum and stored at −20 °C for future use. For PLP/NO coupling, 500 mg of PLGA-NHS and 50 mg of LP/NO (estimated molar ratio = 1:1) were dissolved in 8 mL of DCM and 4 mL of anhydrous methanol, respectively, and mixed together for 100 s. Then, the PLP/NO was immediately precipitated with diethyl ether, washed twice with methanol, dried under vacuum, and stored at −20 °C for future use. The PLP/NO was characterized by ^{1}H nuclear magnetic resonance (NMR) spectroscopy in $CDCl_3$ at 500 MHz using a Varian Unity Inova 500 spectrometer (TOSO, Tokyo, Japan). The FT-IR spectra of PLP/NO were obtained using the same method described above. The distinctive absorption peak of the diazeniumdiolate groups in PLP/NO was measured using the UV/vis spectrophotometer (Optizen 2120 UV, Mecasys) after dissolving it in 1 M NaOH solution and adjusting the pH to 7.

2.3. Nanoparticle Fabrication and Surface Modification. The PLP/NO NPs were fabricated using an oil-in-water (O/W) emulsion solvent evaporation method. Briefly, 100 mg of PLP/NO was dissolved in 5 mL of DCM and poured into 20 mL of ice-cold 2% PVA solution (dissolved in 0.05 M Tris buffer, pH 10). The solution

https://doi.org/10.1021/acsami.1c07407
ACS Appl. Mater. Interfaces 2021, 13, 30383−30396

was probe-sonicated at 150 W for 3 min and stirred at 500 rpm to evaporate the solvent. After residual solvent removal, the PLP/NO NPs were collected by centrifugation (4 °C, 20 000*g*, 30 min) and washed twice with ice-cold distilled water (DW). After washing, the PLP/NO NPs were surface-modified by resuspension in 10 mL of 1% BSA solution and incubation for 10 min. The Alb-PLP/NO NPs were washed twice with ice-cold DW to remove unbound BSA, lyophilized (50 mg of trehalose was added for cryoprotection), and stored at −20 °C for future use. For confocal microscopy and *in vivo* imaging, 1 mg of Nile red and IR780 were added individually to the PLP/NO NPs in DCM solution. To characterize the nanoparticles, their mean hydrodynamic particle size and ζ-potential were measured using a Zetasizer Nano ZS90 (Malvern Instruments, Worcestershire, UK) at pH 7.4. The morphology of the Alb-PLP/NO NPs was assessed using a scanning electron microscope (SEM, Supra 25, Carl Zeiss, Jena, Germany) at an acceleration voltage of 5 kV and transmission electron microscope (TEM; H7600, Hitachi, Tokyo, Japan) at an accelerating voltage of 80 kV. The amount of BSA bound to the surface of the nanoparticles was measured using a Pierce bicinchoninic acid (BCA) protein assay kit (Thermo Fisher Scientific, Rockford, IL) following the manufacturer's instructions.

2.4. NO Release Study. Real-time NO release from the NO-releasing formulations was measured using a Sievers nitric oxide analyzer (NOA 280i, GE Analytical Instruments, Boulder, CO) following a previously reported protocol with some modifications.[50,51] The instrument was calibrated with a 45 ppm of NO gas standard. NO released from the sample was delivered to the instrument at a flow rate of 80 mL/min by Ar gas. To investigate NO release patterns under physiological conditions, the releasing medium [phosphate-buffered saline (PBS) (pH 7.4)] was maintained at 37 °C. The experiments were conducted in the dark to avoid unwanted NO release upon light exposure. After stabilization, each sample was dispersed in DW and added to the releasing medium.

To determine NO loading in the formulations, LP/NO was extracted from the nanoparticles using 0.5 M NaOH solution (for degrading PLGA moiety). Then, the samples were added into the releasing medium consisting of pH 3 citrate buffer (detection range 0.2−2000 nmol of NO). To investigate the presence of diazeniumdiolate groups inside the PLP/NO NPs, the NO release patterns of PLP/NO NPs and PLGA NPs mixed with LP/NO were measured in citrate buffer (pH 3.0) after dispersing in DW.

2.5. Cell Culture. B16F10 murine melanoma cells were purchased from the Korean Cell Line Bank (Seoul, Korea). The cells were grown in DMEM (HyClone, South Logan, UT) supplemented with 10% fetal bovine serum (FBS) (HyClone), penicillin (100 IU/mL, HyClone), and streptomycin (100 μg/mL, HyClone) in the presence of 5% CO_2 at 37 °C.

2.6. Intracellular Delivery of NO. *2.6.1. Quantification of Intracellular NO.* The amount of intracellular NO in B16F10 cells after treatment with LP/NO, PLP/NO NPs, and Alb-PLP/NO NPs was measured using DAF-FM DA.[52] Briefly, the cells were seeded in a 96-well plate at a density of 10 000 cells per well. After overnight incubation, the cell culture medium was replaced with fresh medium, and LP/NO, PLP/NO NPs, or Alb-PLP/NO NPs were added to each well (final concentration adjusted to 100 μM of equivalent NO concentration). After incubating 30 min, the cells were washed three times and incubated with 5 μM DAF-FM-DA for 2 h. Then, the medium was removed, the cells were washed three times, and 100 μL of dimethyl sulfoxide (DMSO) was added. The green fluorescence in each well was measured using a fluorescence multiwell plate reader (Tristar LB 941, Berthold, Germany) at excitation and emission wavelengths of 485 and 520 nm, respectively.

2.6.2. Visualization of Intracellular NO. NO inside the cells was visualized using fluorescence confocal laser scanning microscopy (CLSM) following the manufacturer's protocol with some modifications. Briefly, B16F10 cells were seeded in 4-well chamber slides (SPL Lifesciences, Pocheon, Korea) at a density of 50 000 cells per well and incubated overnight. Next, the medium was replaced with fresh medium, and LP/NO, PLP/NO NPs, or Alb-PLP/NO NPs was added (100 μM of equivalent NO concentration). After incubating 30 min, the cells were washed twice and then incubated with 5 μM DAF-FM-DA for 2 h. Then, the cells were washed three times and counterstained with DAPI solution (5 μg/mL) for 10 min. Afterward, the medium was removed and the cells were imaged using CLSM (FV10, Olympus, Tokyo, Japan) at 60× magnification.

2.7. Cytotoxicity. The cytotoxic effects of the formulations toward B16F10 cells were evaluated using an MTT assay following a previously reported method with some modifications.[53] Briefly, the B16F10 cells were seeded in a 96-well plate at a density of 10 000 cells per well. After overnight incubation, the medium was replaced with fresh medium, and different concentrations of LP/NO, PLP/NO NPs, or Alb-PLP/NO NPs were added to each well. After incubating for 24 h, the medium was replaced with fresh medium containing 1 mg/mL MTT. After incubating for 2 h, the medium was removed, and DMSO was added to dissolve the formazan crystals. The absorbance at 540 nm of each well was measured using a microplate reader (iMark Microplate Reader, Bio-Rad Laboratories, Inc., Richmond, CA). For IC_{50} determinations, the experiments were performed in triplicate, and the IC_{50} values were calculated through nonlinear regression analysis using GraphPad Prism 5 software (GraphPad Software, Inc., La Jolla, CA).

2.8. Tumor Penetration of Alb-PLP/NO NPs. *2.8.1. Evaluation of In Vitro ECM Penetration Effects.* The ECM penetration abilities of PLP/NO NPs and Alb-PLP/NO NPs were evaluated by measuring the maximum migration distance of fluorescence-labeled nanoparticles through a column of mouse ECM extract (Geltrex, ECM extracted from murine Engelbreth−Holm−Swarm (EHS) tumors). Prior to the experiment, the ECM column was prepared by adding 200 μL of ice-cold Geltrex (diluted 10 times in PBS) to the column and incubating at 37 °C for hydrogel formation. After gel formation, IR780-loaded PLP/NO NPs and Alb-PLP/NO NPs were gently added on top of the gel. After incubation at 37 °C for 6 h, the tubes were imaged with an *in vivo* imaging system (IVIS) (FOBI, Neoscience, Suwon, Korea). The maximum migration distance on the IVIS images was measured using ImageJ software (National Institutes of Health, Bethesda, MA).

2.8.2. In Vivo Spatial Distribution of Alb-PLP/NO NPs in Tumors. All animal experiments were reviewed and approved by the Pusan National University Institutional Animal Care and Use Committee (PNU IACUC) on November 25, 2020 (PNU-2020-2804). To investigate the distribution of intratumor-administered PLP/NO NPs and Alb-PLP/NO NPs in melanoma tissue, B16F10-bearing C56BL/6 mice were prepared as an animal model of melanoma. Briefly, 6-week-old C57BL/6 mice were purchased from Samtako Bio (Osan, Korea) and acclimated for 1 week prior to initiation of the experiment. After anesthesia by intraperitoneal administration of 0.5 mg/g of 2,2,2-tribromoethanol, 10^6 B16F10 cells were subcutaneously injected in the upper flank of the right hind leg of each mouse after hair removal in the area. The length (L) and width (W) of each tumor were measured using digital calipers, and the tumor volume (V) was calculated using the following formula: $V = (L \times W^2)/2$.[54] When the tumor volume was ∼1000 mm^3, IR780-loaded PLP/NO NPs and Alb-PLP/NO NPs were intratumorally injected under anesthesia. Six hours later, the mice were euthanized, and each tumor was excised. The tumors were gently washed and fixed in 10% formalin solution containing 4% sucrose for 6 h. After fixation, the excised tumors and their cross-sectioned hemispheres were imaged using an IVIS.

For quantitative evaluation of spatial distribution, Nile red-loaded PLP/NO NPs and Alb-PLP/NO NPs were injected intratumorally, and the tumors were excised following the above-mentioned method. After fixation, the tumors were cut into 48 pieces; each piece was embedded in FSC 22 frozen section media (Leica Microsystems, Wetzlar, Germany) and then stored at −75 °C for future use. For visualization, 5-μm-thick slices of each piece were produced using a cryotome (Leica CM1860, Leica Microsystems), the cell nuclei were stained with DAPI, and a representative confocal image of each piece was acquired using CLSM. The number of red-fluorescence-positive sections (nanoparticle-presenting areas) was counted, and the ratio of this number to the total number of sections was calculated to evaluate the tumor penetration effects of the nanoparticles.

https://doi.org/10.1021/acsami.1c07407
ACS Appl. Mater. Interfaces 2021, 13, 30383−30396

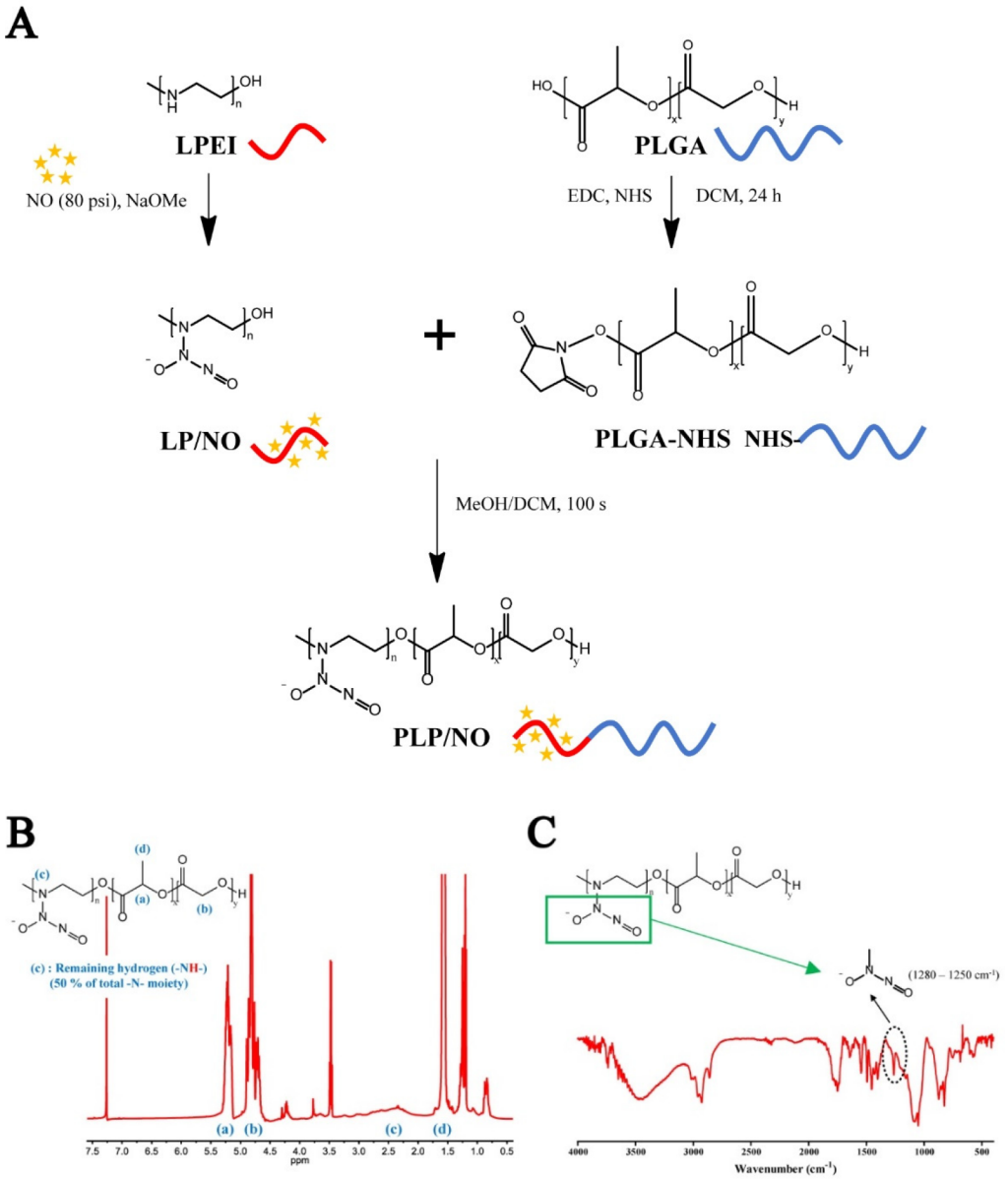

Figure 1. Synthesis and characterization of PLP/NO. (A) Schematic diagram of PLP/NO synthesis. (B) ^{1}H NMR spectrum of PLP/NO in $CDCl_3$ at 500 MHz. (C) FT-IR spectrum of PLP/NO.

2.9. *In Vivo* Antitumor Assay. The *in vivo* antitumor activity of Alb-PLP/NO NPs was investigated in the B16F10-bearing C57BL/6 mouse model. B16F10 tumors were produced by the method described in section 2.8.2. When the tumor volume reached ~150 mm^3, the mice were randomly assigned to five groups: untreated, Alb-PLP NPs, LP/NO, PLP/NO NPs, and Alb-PLP/NO NPs. Every 2 days, under anesthesia, body weights and tumor sizes were measured as representative parameters of systemic toxicity and disease severity. The formulations were administered intratumorally with an NO equivalent of 6.6 μmol/kg after tumor size measurement. The specific growth rate (SGR) of each tumor was calculated using the following formula: SGR = ΔLog $V/\Delta t$, where t is the time in days.[55] Eight days after treatment initiation, all mice were euthanized, and their tumors were excised. For histological examination, hematoxylin and eosin (H&E) and terminal deoxynucleotidyl transferase-deoxyuridine triphosphate nick end labeling (TUNEL) staining were conducted. Briefly, the excised tumors were immediately immersed in 10% formalin containing 4% sucrose for 12 h. After an additional incubation using 30% sucrose for 24 h, the tumors were embedded and sectioned by the same method as described in section 2.8.2. Each staining protocol was performed according to the manufacturer's instructions. The H&E-stained images were acquired using a BX53 light microscope (Olympus), and the TUNEL-stained images were acquired using an LSM 800 confocal microscope (Carl Zeiss, Oberkochen, Germany). The areas of the necrotic zone in tumor tissues treated with PLP/NO NPs and Alb-PLP/NO NPs were calculated from the three different H&E images obtained for each group using the ImageJ software (National Institutes of Health, Bethesda, MD).

2.10. Statistical Analysis. All statistical analyses were performed using GraphPad Prism 5.0 (GraphPad Software, Inc.) with two-tailed *t*-tests, one-way ANOVA, or two-way ANOVA followed by Tukey or Bonferroni post-tests to determine the differences of means among groups. *P*-Values less than 0.05 were considered statistically significant.

3. RESULTS AND DISCUSSION

3.1. Synthesis and Characterization of PLP/NO. LPEI diazeniumdiolate (LP/NO) was prepared by direct addition of NO to the secondary amine moieties of LPEI, as shown in

https://doi.org/10.1021/acsami.1c07407
ACS Appl. Mater. Interfaces 2021, 13, 30383−30396

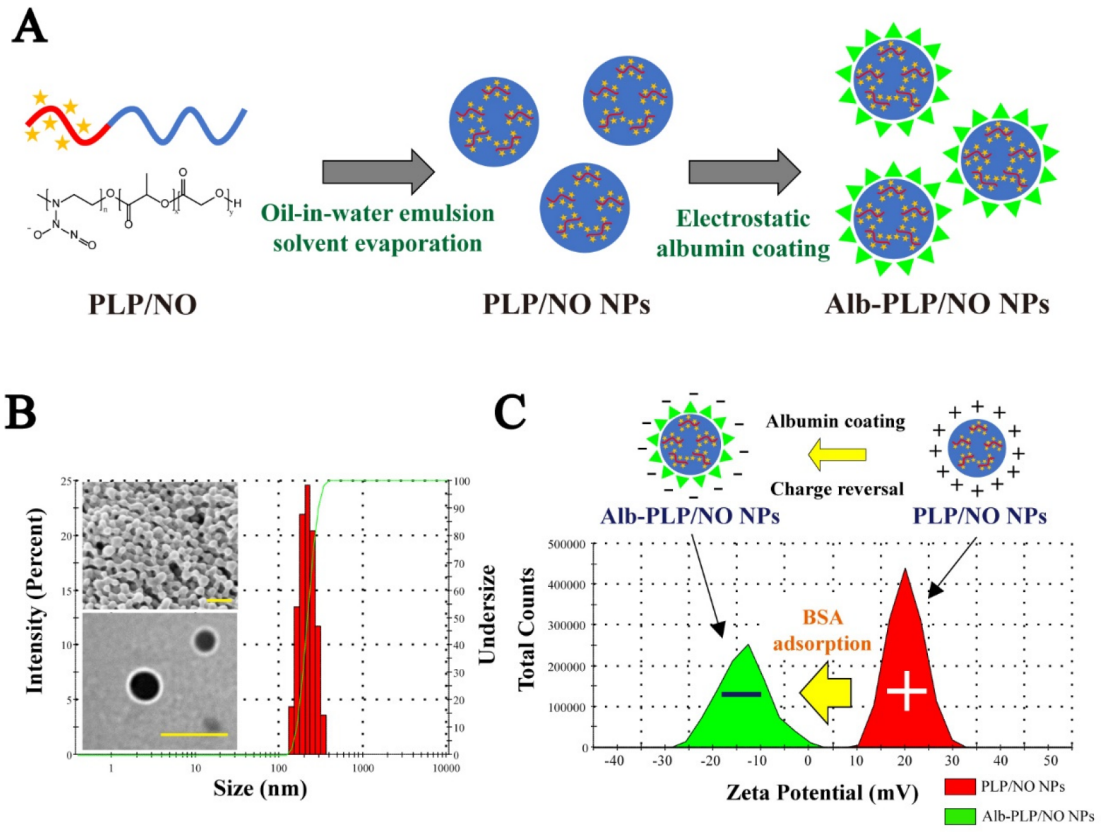

Figure 2. Fabrication scheme and characterization of PLP/NO NPs and Alb-PLP/NO NPs. (A) Schematic illustration of the fabrication of Alb-PLP/NO NPs. (B) Hydrodynamic particle size distribution and representative SEM and TEM images of Alb-PLP/NO NPs. Scale bar represents 0.5 μm. (C) ζ-Potential distribution of PLP/NO NPs and Alb-PLP/NO NPs at pH 7.4.

Figure 1A. LP/NO showed the characteristic absorption peak of diazeniumdiolate groups at ~245 nm, the amplitude of which was concentration-dependent, indicating successful diazeniumdiolate formation [Figure S1A, Supporting Information (SI)]. The synthesis of LP/NO was also confirmed by FT-IR analysis, with the characteristic stretch from the diazeniumdiolate group observed at 1280−1250 cm^{-1} (Figure S1B, SI). The amount of NO loading was quantified from three different batches of LP/NO using the NOA 280i instrument and was found to be 7.2 ± 0.8 μmol NO/mg of LP/NO.

After LP/NO preparation, PLP/NO was synthesized by an esterification reaction between the terminal hydroxyl group of LP/NO and PLGA-NHS prepared by activation of the terminal carboxyl group of PLGA (Figure 1A). Because of the poor solubility of LP/NO in DCM caused by increased hydrophilicity after diazeniumdiolate formation, the reaction was conducted in methanol:DCM (1:2, v/v), which was able to maintain both LP/NO and PLGA-NHS in solution. The reaction time was optimized to 100 s through a series of pilot studies because long-term exposure of LP/NO to PLGA leads to hydrolysis of PLGA under the reaction conditions due to the highly basic nature of LP/NO. Optimization of the synthesis of PLP/NO resulted in a yield of 99%.

Next, the synthesized PLP/NO was characterized by ^{1}H NMR and FT-IR. In the ^{1}H NMR spectrum of PLP/NO, characteristic peaks from both the PLGA and LP/NO moieties were observed (Figure 1B). Moreover, in the ^{1}H NMR spectra of PLP and PLP/NO, the peak from the repeating unit of LPEI (−NH−) (δ = 1.71 ppm, peak e) was downfield-shifted (δ = 2.17 ppm, peak g; δ = 2.34 ppm, peak j) owing to the deshielding effects provided by the increased intermolecular hydrogen bonding with oxygen atoms of the PLGA moiety (Figure S2A, SI). In the ^{1}H NMR spectrum of PLP/NO, compared with that of PLP, a broader and smaller, downfield-shifted peak was observed because ~25% of the total hydrogen molecules of the (−NH−) moieties were substituted with diazeniumdiolates, which are strong electron-withdrawing groups. A stretch peak was observed in the FT-IR spectrum of PLP/NO at a wavenumber of 1280−1250 cm^{-1} (Figure 1C), indicating that the diazeniumdiolate groups were maintained after PLP/NO synthesis. Moreover, the presence of diazeniumdiolate groups in PLP/NO was also confirmed by UV/vis spectroscopy; the characteristic absorption peak was observed at a wavelength of 245 nm with a concentration-dependent amplitude (Figure S2B, SI). This stability was due to the use of nonaqueous solvents and short reaction times that prevented diazeniumdiolate hydrolysis.

3.2. Fabrication and Characterization of Alb-PLP/NO NPs. The albumin-coated PLP/NO NPs (Alb-PLP/NO NPs) were successfully fabricated via an O/W emulsion solvent evaporation method followed by surface modification with BSA (Figure 2A). Since the diazeniumdiolate groups of PLP/NO are easily hydrolyzed at a high temperature or under acidic and neutral pH conditions, a basic pH (pH 10) and ice-cold temperature were maintained to minimize the unwanted release of NO during fabrication of the nanoparticles. After fabrication of the PLP/NO NPs, BSA was adsorbed on their surface through the electrostatic interaction between the negatively charged BSA and positively charged PLP/NO NPs at pH 7.4. After surface modification, the hydrodynamic

https://doi.org/10.1021/acsami.1c07407
ACS Appl. Mater. Interfaces 2021, 13, 30383−30396

Table 1. Physicochemical Characteristics of the Nanoparticles

	size (nm)	polydispersity index (PDI)	ζ-potential (mV)	NO loading (μmol/mg)
PLP NPs	221.8 ± 6.9	0.176 ± 0.04	14.6 ± 0.4	
PLP/NO NPs	213.2 ± 5.0	0.097 ± 0.05	15.6 ± 0.4	0.35 ± 0.04
Alb-PLP NPs	224.4 ± 1.8	0.087 ± 0.06	−10.1 ± 1.5	
Alb-PLP/NO NPs	215.5 ± 3.2	0.104 ± 0.08	−8.5 ± 0.5	0.34 ± 0.03

Table 2. NO Release Properties of LP/NO, PLP/NO NPs, and Alb-PLP/NO NPs[a]

	$[NO]_T$ (μmol/mg)	$[NO]_{max}$ (ppb/mg)	$t_{[NO]_{max}}$ (h)	$t_{1/2}$ (h)	t_d (h)
LP/NO	7.15 ± 0.80	3304.7 ± 9.0	0.10 ± 0.01	1.46 ± 0.18	11.18 ± 0.28
PLP/NO NPs	0.35 ± 0.04	392.7 ± 15.7	0.16 ± 0.02	2.24 ± 0.20	20.67 ± 0.53
Alb-PLP/NO NPs	0.34 ± 0.03	374.8 ± 20.6	0.13 ± 0.03	2.27 ± 0.12	21.80 ± 0.37

[a] $[NO]_T$: total NO release. $[NO]_{max}$: maximum NO flux. $t_{[NO]_{max}}$: time to reach $[NO]_{max}$. $t_{1/2}$: half-life of NO release. t_d: duration time (time when 99% of NO is released). Results are presented as means ± standard deviations (n = 3).

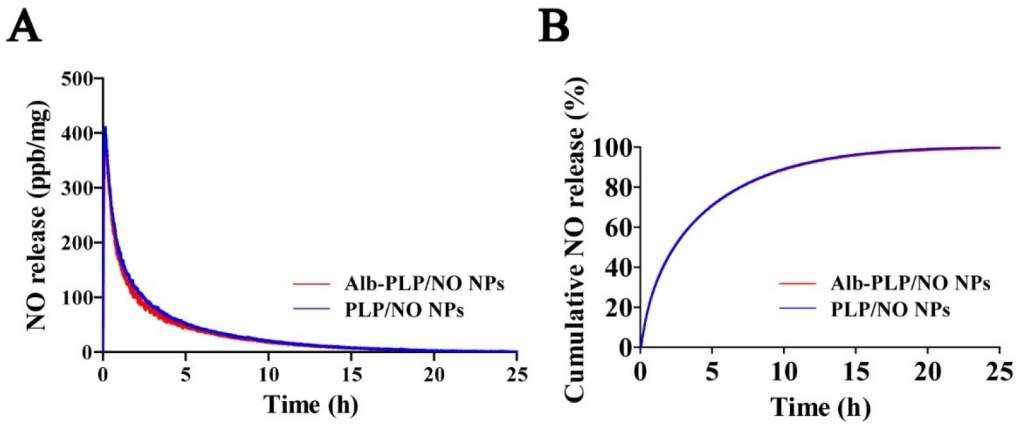

Figure 3. NO release profiles of PLP/NO NPs and Alb-PLP/NO NPs. (A) Real-time NO release profiles of PLP/NO NPs and Alb-PLP/NO NPs in pH 7.4 buffer at 37 °C. (B) Cumulative NO release profiles of PLP/NO NPs and Alb-PLP/NO NPs in pH 7.4 buffer at 37 °C.

particle size, ζ-potential, and NO-loading of the Alb-PLP/NO NPs were measured (Figure 2, Table 1). The particles were spherical in shape in SEM images, and the average hydrodynamic particle size was 215.5 ± 3.2 nm with a narrow size distribution (polydispersity index (PDI): 0.104 ± 0.08) (Figure 2B). In addition, owing to the successful adsorption of BSA, 20.5 ± 3.3 nm of corona was observed around the surface of the nanoparticles by TEM (Figure 2B). The amount of bound BSA was measured via BCA protein assay, and an amount of BSA equivalent to 5.96 ± 0.53% of the total particle weight was bound to the surface of Alb-PLP/NO NPs. The albumin coating did not increase the mean hydrodynamic particle size of the nanoparticles (PLP/NO NPs vs Alb-PLP/NO NPs: 213.2 ± 5 vs 215.5 ± 3.2 nm, not statistically significant), which may have been caused by the attenuation of mild particle aggregation due to the increased colloidal stability of the albumin coat. Hyun et al. also reported that there is no significant difference in particle size between albumin-coated PLGA nanoparticles (185 ± 16 nm) and uncoated PLGA nanoparticles (188 ± 13 nm).[46] The amount of NO loading was also similar between the PLP/NO NPs and Alb-PLP/NO NPs (0.35 ± 0.04 and 0.34 ± 0.03 μmol/mg, respectively), indicating that the albumin-coating process had no effect on NO loading. The encapsulation efficiency (EE) was ∼64% of the theoretical NO loading, suggesting that 36% of the NO was prematurely released during the nanoparticle fabrication processes. Unlike particle size and NO loading, the ζ-potentials of the PLP/NO NPs and Alb-PLP/NO NPs were very different (+15.6 ± 0.4 and −8.5 ± 0.5 mV, respectively) due to the adsorption of negatively charged BSA on the positively charged surface of the PLP/NO NPs, which is attributed to the secondary amine moiety of PLP/NO (Figure 2C). The ζ-potential values remained constant after several washes, suggesting that the BSA molecules were bound to the surface of the PLP/NO NPs via electrostatic interactions that were not easily disrupted. Taken together, the Alb-PLP/NO NPs and PLP/NO NPs showed similar hydrodynamic particle sizes and NO loading, but the surface charge of the former was negative from the adsorption of BSA.

3.3. NO Release Study. The NO release profiles of LP/NO, PLP/NO NPs, and Alb-PLP/NO NPs were evaluated by measuring real-time NO release using the NOA 280i. Half-life ($t_{1/2}$, time when 50% of the NO has been released), duration time (t_d, time when 99% of the NO has been released), total amount of NO ($[NO]_T$), momentary maximum NO flux ($[NO]_{max}$), and time to reach $[NO]_{max}$, ($t_{[NO]_{max}}$) were calculated to evaluate the NO release patterns. Since PLP/NO is not soluble in aqueous medium, the analysis of NO release from PLP/NO could not be conducted using the NOA instrument. Under physiological conditions, LP/NO released NO for 11.18 ± 0.28 h with a $t_{1/2}$ of 1.46 ± 0.18 h [Table 2 and Figure S3A (SI)]. Both PLP/NO NPs and Alb-PLP/NO NPs released NO for more than 20 h following similar first-order kinetics (t_d, 20.67 ± 0.53 and 21.8 ± 0.37 h; $t_{1/2}$, 2.24 ± 0.20 and 2.27 ± 0.12 h, for PLP/NO NPs and Alb-PLP/NO

https://doi.org/10.1021/acsami.1c07407
ACS Appl. Mater. Interfaces 2021, 13, 30383−30396

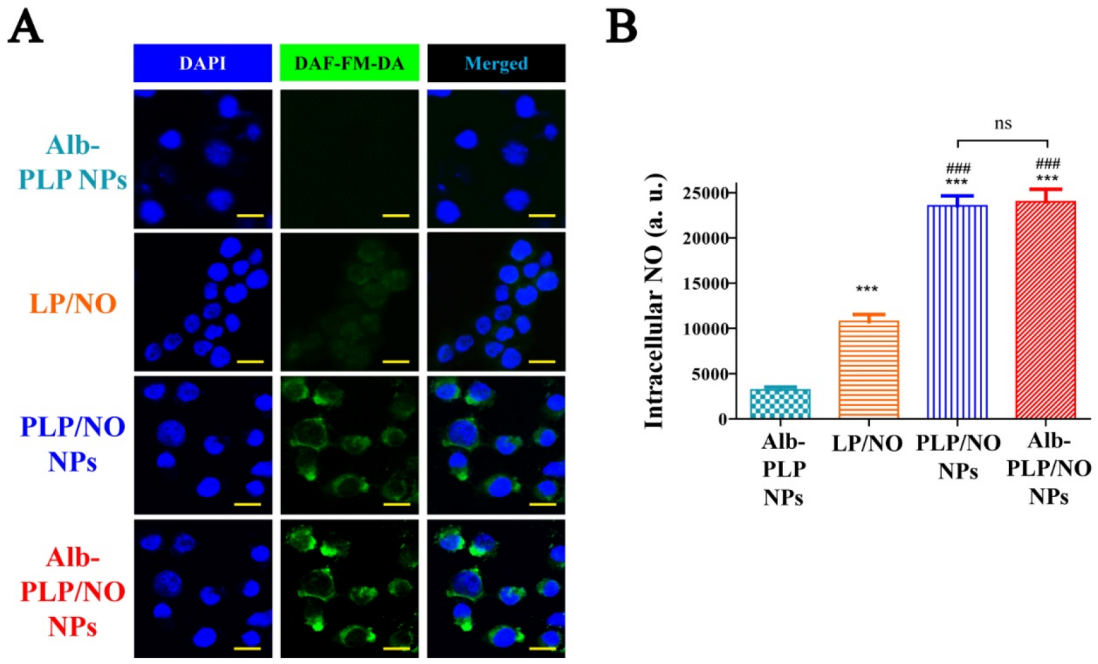

Figure 4. Measurement of intracellular NO delivery in B16F10 cells after treatment with Alb-PLP NPs, LP/NO, PLP/NO NPs, and Alb-PLP/NO NPs. (A) Representative confocal laser scanning microscopy (CLSM) images of B16F10 cells treated with the formulations. Blue and green colors indicate DAPI and DAF-FM/NO, respectively. The scale bar represents 10 μm. (B) Fluorescence intensity of DAF-FM/NO measured by a fluorescence microplate reader. The data represent means ± standard deviations (n = 6, ***P < 0.001 compared to the Alb-PLP NPs group, $^{\#\#\#}P$ < 0.001 comparted to the LP/NO group. ns: not significant).

NPs, respectively) (Table 2 and Figure 3). The albumin coating on the surface of the PLP/NO NPs did not significantly affect the NO release pattern of the nanoparticles. Although albumin can act as a NO reservoir via the formation of *S*-nitroso albumin,[56] the thin coating of BSA on the surface of the PLP/NO NPs was not sufficient to significantly alter NO release. The prolonged duration of NO release from the PLP/NO NPs and Alb-PLP/NO NPs compared with that of LP/NO can be explained by the lower rate of hydrolysis of the diazeniumdiolate groups in the nanoparticles. Since the diazeniumdiolate groups inside the nanoparticles are protected from the external aqueous medium, the release of NO from the nanoparticles due to diazeniumdiolate group hydrolysis would be slow and sustained (Figure S3B, SI). A sufficient duration of NO release is important for a local antimelanoma therapeutic to deliver NO to the target site (cancer cells) since it takes time after administration to reach the cancer cells located beyond dense ECM networks. Otherwise, all of the NO would be prematurely released before reaching the target cells, resulting in delivery failure. Thus, in this study, a formulation that releases NO for more than 21 h was developed by synthesizing PLP/NO, followed by nanoparticle fabrication and albumin coating. The NO release profile of the Alb-PLP/NO NPs indicates that they could exert antimelanoma effects by efficiently delivering NO because of their high NO loading and sustained NO release.

3.4. Intracellular Delivery of NO. Since NO exerts its cytotoxic effects by interacting with various cell components, the amount of intracellular NO is strongly associated with cytotoxicity. Thus, efficient NO delivery into cancer cells is essential to achieve potent cytotoxic effects using NO-releasing formulations. To evaluate the efficiency of the intracellular NO delivery of the LP/NO, PLP/NO NPs, and Alb-PLP/NO NPs, the level of NO inside the cells after exposure to the formulations was measured using DAF-FM-DA. Green fluorescence from the cell-membrane-impermeable DAF-FA/NO, which is a stoichiometric reaction product of NO and DAF-FM-DA, was measured and imaged after removal of the medium to quantify the amount of NO delivered into the cells. After a 30 min incubation, distinct green fluorescence, indicative of intracellular NO, was observed near the nucleus in the CLSM images of the PLP/NO NP- and Alb-PLP/NO NP-treated groups, while negligible green fluorescence was observed in the groups treated with LP/NO and albumin-coated PLP NP (Alb-PLP NP) (Figure 4A). Although the same NO equivalent was used, only a dim green fluorescence could be observed in the LP/NO-treated group. The signals were quantified using a microplate reader and the results revealed that the PLP/NO NP- and Alb-PLP/NO NP-treated groups had more than 7 times higher fluorescence intensity than the Alb-PLP NP-treated group (Figure 4B). In addition, the signals from the PLP/NO NP- and Alb-PLP/NO NP-treated groups were more than 2 times stronger than that of the LP/NO-treated group. Unlike with the CLSM imaging results, the LP/NO-treated group exhibited 3 times the fluorescence intensity of the Alb-PLP NP-treated group. Owing to low fluorescence intensities and imaging detection limits, it was difficult to distinguish the fluorescence of the Alb-PLP NP- and LP/NO-treated groups with CLSM imaging. Since a limited amount of LP/NO could be attached to the surface of the cells and release NO before internalization, a limited amount of NO could be delivered into the cells by this treatment. In contrast, the PLP/NO NPs and Alb-PLP/NO NPs can be easily internalized by nonspecific endocytosis[57] and albumin-receptor-mediated endocytosis[58,59] to release NO in the cells; thus, more than twice the amount of NO could be delivered into the cells compared with that from LP/NO. The enhanced delivery efficiency of the PLP/NO NPs and Alb-

https://doi.org/10.1021/acsami.1c07407
ACS Appl. Mater. Interfaces 2021, 13, 30383−30396

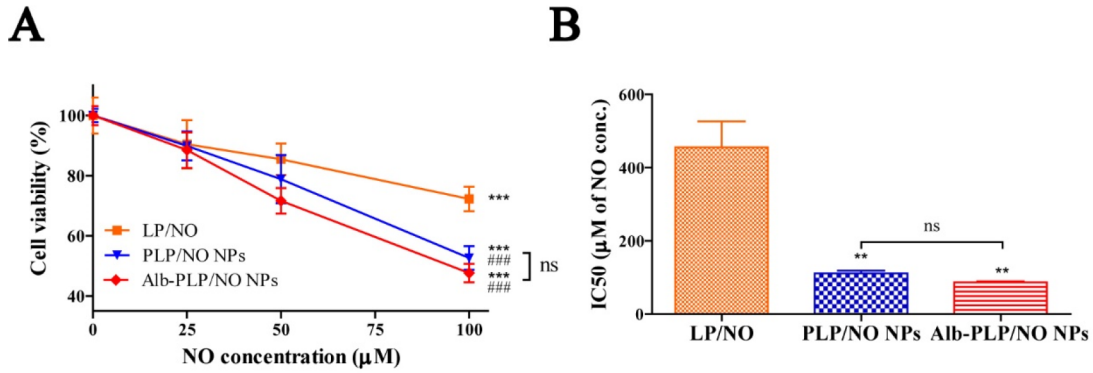

Figure 5. Cytotoxicity of LP/NO, PLP/NO, and Alb-PLP/NO NPs in B16F10 cells assessed by the MTT assay. (A) Cytotoxic effects of LP/NO, PLP/NO NPs, and Alb-PLP/NO NPs at various NO equivalent concentrations after 24-h incubation (n = 4, ***P < 0.001 compared to the Alb-PLP NPs group and $^{\#\#\#}P$ < 0.001 compared to the LP/NO group). (B) IC_{50} of LP/NO, PLP/NO NPs, and Alb-PLP/NO NPs in B16F10 cells after 24-h incubation (455.5 ± 122.1, 134.9 ± 15.5, and 97.1 ± 6.1 μM of NO concentration for LP/NO, PLP/NO NPs, and Alb-PLP/NO NPs, respectively). Results are expressed as means ± standard deviations (n = 3, **P < 0.01 compared to LP/NO group. ns: not significant).

PLP/NO NPs may have resulted from the properties of the nanoparticle formulations that enable them to be internalized via endocytosis (Figure S4, SI). The NO delivery efficiencies of the PLP/NO NPs and Alb-PLP/NO NPs were similar, indicating that the albumin coating did not reduce the efficiency of NO delivery. These results suggest that the Alb-PLP/NO NPs can deliver sufficient quantities of NO into melanoma cells to produce potent antimelanoma effects.

3.5. *In Vitro* Cytotoxicity of Nanoparticles in Melanoma Cells. The cytotoxicity of Alb-PLP NPs, LP/NO, PLP/NO NPs, and Alb-PLP/NO NPs was evaluated in B16F10 murine melanoma cells using an MTT assay. As shown in Figure 5, all NO-releasing formulations (LP/NO, PLP/NO NPs, and Alb-PLP/NO NPs) exhibited concentration-dependent cytotoxic activity. The Alb-PLP NPs did not show any cytotoxic effect, indicating that the toxicity of the Alb-PLP/NO NPs resulted from released NO and not from the nanoparticles themselves. In addition, since the Alb-PLP/NO NPs would be converted to Alb-PLP NPs after releasing their NO stores, local antimelanoma therapy could be achieved by the local administration of Alb-PLP/NO NPs without the risk of systemic toxicity. The PLP/NO NPs and Alb-PLP/NO NPs exhibited more potent cytotoxic effects than LP/NO with IC_{50} values of 455.5 ± 122.1, 134.9 ± 15.5, and 97.1 ± 6.1 μM of NO concentration for LP/NO, PLP/NO NPs, and Alb-PLPNO NPs, respectively. In Figure 4, we showed that the NP formulations could enhance intracellular delivery of NO. Thus, the cytotoxicity caused by NO delivery into the cells was stronger with the PLP/NO NPs and Alb-PLP/NO NPs than with LP/NO. However, there was no significant difference in cytotoxicity between the PLP/NO NPs and Alb-PLP/NO NPs due to similar levels of intracellular NO between the two treatments.

3.6. Tumor Penetration Ability of Alb-PLP/NO NPs. The tumor ECM consists of three-dimensional networks of various macromolecules, such as collagen, fibronectin, laminin, and hyaluronic acid. The ECM is one of the major obstacles that limit the therapeutic efficacy of nanoparticle formulations by hindering their diffusion to cancer cells in the tumor tissue.[33] ECM penetration is a crucial factor affecting antitumor activity because restricted access to the cancer cells reduces drug efficacy by limiting drug delivery. Accordingly, the absence of ECM in 2D cell culture models is considered to be one of the main reasons that several nanoparticle formulations that exhibited potent cytotoxicity in tumor cell culture failed to demonstrate *in vivo* antitumor activity.[60]

In this study, we investigated the ECM-penetrating ability of the PLP/NO NPs and Alb-PLP/NO NPs by measuring the maximum migration distance of the nanoparticles through an ECM. As shown in Figure 6A, the albumin surface modification substantially enhanced the ability to penetrate the ECM; the maximum migration distance was 2.94 ± 1.24 and 8.77 ± 0.59 mm for the PLP/NO NPs and Alb-PLP/NO NPs, respectively. Considering the fact that there was no significant difference in particle size between the two formulations (Table 1), the 3-fold higher maximum migration distance of the Alb-PLP/NO NPs can be attributed solely to the presence of albumin on the particle surface. This can be explained by the surface charge adjustment provided by the albumin coating. ECM penetration of the positively charged PLP/NO NPs (+15.6 ± 0.4 mV ζ-potential) was limited because the increased electrostatic forces between the positively charged nanoparticles and negatively charged ECM components would restrict diffusion of the former.[45,61] Conversely, repulsive forces would be generated between the negatively charged Alb-PLP/NO NPs (−8.5 ± 0.5 mV ζ-potential) and negatively charged ECM, enhancing migration and ECM penetration. The effect of ECM penetration on the treatment of melanoma could be even more important with NO-based nanoparticles than with conventional chemotherapeutic-loaded nanoparticles. Since NO released from the nanoparticles is able to diffuse only a short distance (40−200 μm in a few seconds) and it quickly loses its activity,[35] NO-releasing nanoparticles bound by the ECM cannot deliver sufficient NO quantities to the entire tumor tissue, resulting in decreased anticancer activity. Therefore, by increasing the ECM-penetrating ability via albumin coating, accessibility of the Alb-PLP/NO NPs to the cancer cells is increased, resulting in enhanced NO delivery to the entire tumor tissue.

Next, we determined the spatial distribution of the nanoparticles in the tumor tissue to evaluate *in vivo* tumor penetration. First, 6 h after intratumoral administration of IR780-loaded PLP/NO NPs and Alb-PLP/NO NPs, the tumors were excised and imaged using an IVIS. As shown in Figure 6B, fluorescence was observed in approximately 75% of whole tumor images with the Alb-PLP/NO NPs and approximately 40% with the PLP/NO NPs. After whole

https://doi.org/10.1021/acsami.1c07407
ACS Appl. Mater. Interfaces 2021, 13, 30383−30396

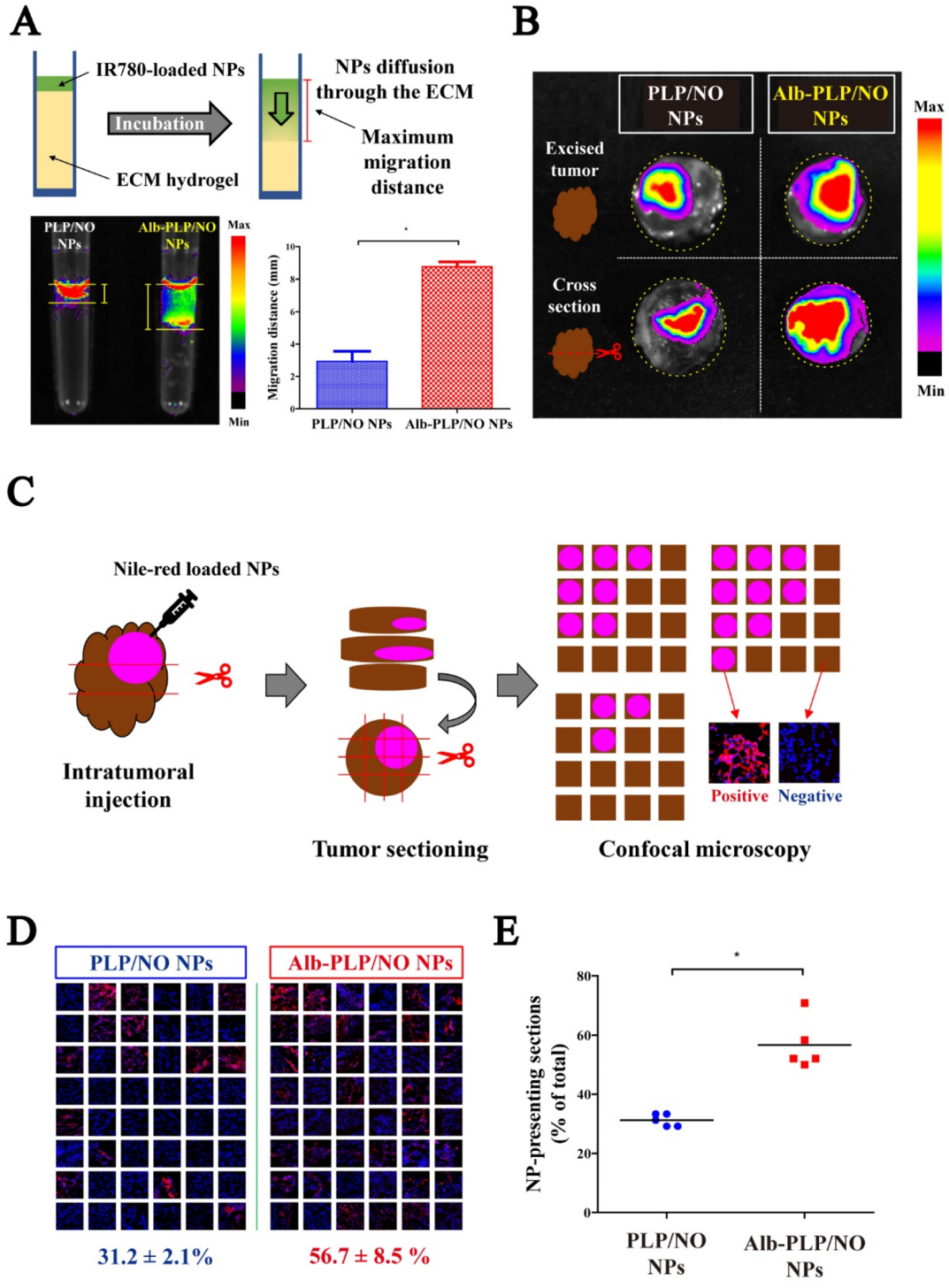

Figure 6. Evaluation of the ECM penetration ability of PLP/NO NPs and Alb-PLP/NO NPs. (A) Schematic illustration of the *in vitro* ECM penetration experiment, representative fluorescence images of the ECM column overlaid with IR780-loaded PLP/NO NPs and Alb-PLP/NO NPs, and the maximum migration distance of the nanoparticles. Data are presented as means ± standard deviations (n = 3, *P < 0.05 compared to the PLP/NO NPs group). (B) Representative IVIS images of excised B16F10 tumors and their cross-sectional planes. Images were taken 6 h after intratumoral administration of IR780-loaded PLP/NO NPs and Alb-PLP/NO NPs. (C) Schematic illustration of the spatial distribution test after intratumoral administration of Nile red-loaded PLP/NO NPs and Alb-PLP/NO NPs. (D) Representative CLSM images from each fragment of the tumor treated with Nile red-loaded PLP/NO NPs and Alb-PLP/NO NPs. (E) Percentage of sections exhibiting red fluorescence. Horizontal bars represent means (n = 5, *P < 0.05 compared to the PLPNO NPs group).

tumor imaging, cross-sectional planes of the tumors were also imaged using the IVIS. It is worth noting that whole tumor imaging cannot precisely analyze the internal distribution of nanoparticles because fluorescence from deep inside the tumor is quenched by black-colored melanin produced by melanoma cells. In the tumor images, fluorescence in the Alb-PLP/NO NP-treated group encompassed ∼92% of the cross-sectional plane of the tumor, while this value was ∼31% for the PLP/

https://doi.org/10.1021/acsami.1c07407
ACS Appl. Mater. Interfaces 2021, 13, 30383−30396

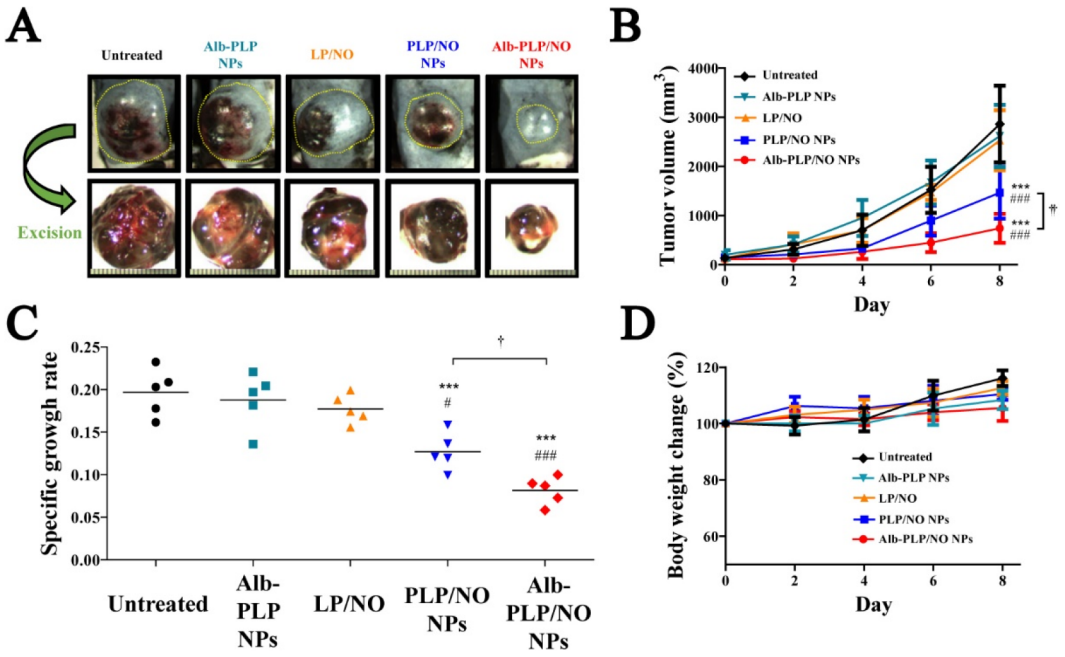

Figure 7. *In vivo* antitumor effects of NO-releasing formulations in the B16F10-bearing mouse model (n = 5). (A) Representative macroscopic images of tumors 8 days after treatment initiation. (B) Tumor growth profiles after treatment initiation. Results are expressed as means ± standard deviations. (C) Specific growth rate of each tumor. Horizontal bars represent the means. (D) Body weight changes after treatment initiation. Results are expressed as means ± standard deviations. ***P < 0.001 compared to the untreated group, $^{\#}P$ < 0.05 and $^{\#\#\#}P$ < 0.001 compared to the LP/NO group, and $^{\dagger}P$ < 0.05 and $^{\dagger\dagger}P$ < 0.01 compared to the PLP/NO NPs group.

NO NP-treated group. There was no significant difference in tumor penetration effect between particles without NO (PLP NPs and Alb-PLP NPs) and those with NO (PLP/NO NPs and Alb-PLP/NO NPs), indicating that tumor penetration of the nanoparticles is affected only by the albumin coating and not by the presence of NO (Figure S6, SI).

To investigate the spatial distribution of the nanoparticles further, the tumors were sectioned into 48 pieces, and the presence of red fluorescent nanoparticles in each piece was examined using CLSM (Figure 6C). We found that 56.7 ± 8.5% and 31.2 ± 2.1% of the sections were positive for red fluorescence in the Nile red-loaded Alb-PLP/NO NP-treated and PLP/NO NP-treated groups, respectively (Figure 6D,E). These results are consistent with those from the *in vitro* ECM penetration study discussed earlier in this section. Since diffusion of positively charged PLP/NO NPs through the ECM network was restricted, their spatial distribution was also limited in B16F10-bearing tumors possessing a dense ECM. In contrast, owing to the reduced electrostatic interactions with the ECM caused by the albumin coating, the Alb-PLP/NO NPs showed a widespread spatial distribution to the entire tumor tissue, resulting in increased NO delivery.

3.7. *In Vivo* Antitumor Activity. To investigate the inhibitory effects of LP/NO, PLP/NO NPs, and Alb-PLP/NO NPs on tumor growth, the B16F10 murine melanoma cell bearing C57BL/6 mouse was used as an animal model of melanoma. Each formulation was administered intratumorally every 2 days to avoid the stress caused by frequent anesthesia and injection. Compared with the untreated group, the PLP/NO NPs and Alb-PLP/NO NPs significantly inhibited tumor growth, while LP/NO and the Alb-PLP NPs did not (Figure 7). In particular, the Alb-PLP/NO NP-treated group exhibited the most potent antitumor effect and showed significantly stronger tumor growth inhibition than the PLP/NO NP-treated group did (Figure 7B). Intratumoral administration of LP/NO with an NO equivalent of 6.6 μmol/kg did not exhibit significant antitumor activity, possibly due to the low delivery efficiency of NO and higher IC_{50} of LP/NO (Figures 4 and 5). To evaluate the growth inhibition efficacy of the NO-releasing formulations, SGR, a parameter for assessing the exponential growth of tumors,[55] was calculated from the time−tumor volume profiles. As shown in Figure 7C, the PLP/NO NP- and Alb-PLP/NO NP-treated groups showed significantly lower SGR than the untreated groups, while the SGR of the Alb-PLP NP- and LP/NO-treated groups was not significantly different. The SGR of the Alb-PLP/NO NPs was significantly lower than that of the PLP/NO NPs; the enhanced inhibitory effect of the Alb-PLP/NO NPs on tumor growth resulted from their increased tumor penetration compared with that of the PLP/NO NPs. Since the Alb-PLP/NO NPs can distribute to a larger volume of the tumor than the PLP/NO NPs, more melanoma cells were exposed to NO with the former nanoparticles, resulting in enhanced antitumor effects.

To investigate the systemic toxicity of the intratumorally administered formulations, body weight changes were monitored during the experiment. Compared with the healthy group, none of the groups showed significant body weight reductions (Figure 7D). Owing to the short diffusible distance of NO, its cytotoxic effects would be limited to the local tumor tissue, resulting in minimal off-target systemic toxicity. Thus, NO-based therapeutics could be desirable formulations for the local treatment of melanoma since potential toxicity cannot be excluded using traditional chemotherapeutic formulations.

To understand the enhanced antitumor effects of the Alb-PLP/NO NPs further, H&E staining and TUNEL staining were conducted to evaluate morphological changes and the presence of apoptotic cells, respectively, in the tumors treated with the formulations. H&E staining revealed that the area of

https://doi.org/10.1021/acsami.1c07407
ACS Appl. Mater. Interfaces 2021, 13, 30383−30396

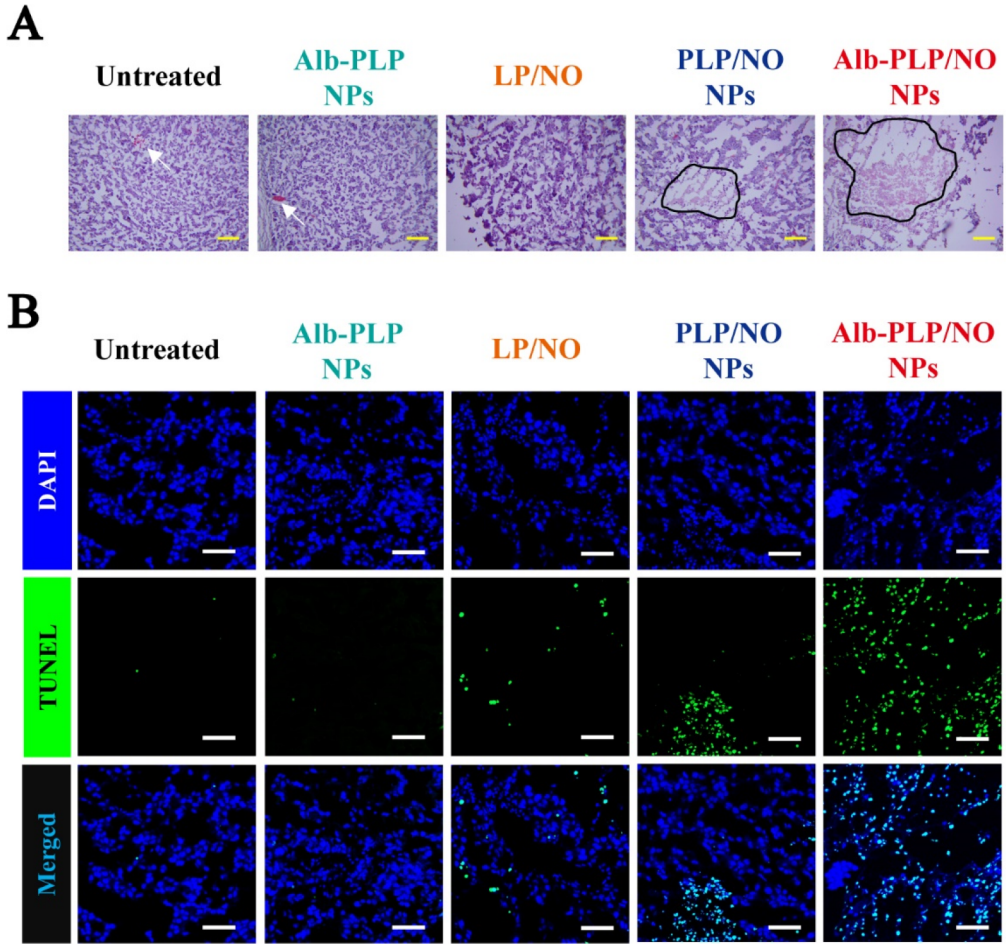

Figure 8. Histological examination of tumor sections on day 8. (A) Representative microscopic images of H&E-stained tumor sections. White arrows point to tumor blood vessels, circled areas indicate necrotic zones, and the yellow scale bar represents 100 μm. (B) Representative CLSM images of tumor sections after terminal deoxynucleotidyl transferase-deoxyuridine triphosphate nick end labeling (TUNEL) staining. The scale bar represents 50 μm.

the necrotic zone in tumor tissues from the Alb-PLP/NO NP-treated group was approximately 3-fold larger than that from the PLP/NO NP group [Figures 8A and S7 (SI)]. The results suggest that treatment with Alb-PLP/NO NPs enhanced tumor growth inhibition via cytotoxic effects to a larger region than treatment with PLP/NO NPs, an effect caused by the enhanced tumor penetration of the Alb-PLP/NO NPs. H&E images of the LP/NO- and Alb-PLP NP-treated tumors (and those from the untreated group) did not show detectable necrotic zones. In addition, owing to tumor angiogenesis, blood vessels were observed in the H&E images of Alb-PLP NP-treated and untreated tumors.

To evaluate the extent of apoptosis in the tumors, TUNEL assays were conducted on day 8. As shown in Figure 8B, higher numbers of TUNEL-positive cells (green fluorescence) were observed in the Alb-PLP/NO NP-treated tumors than in tumors from the other experimental groups. In the TUNEL-stained images of the PLP/NO NP-treated tumors, TUNEL-positive cells were observed in a narrow region due to limited diffusion of the PLP/NO NPs in the tumors. Apoptotic cells were also observed in the TUNEL-stained images of LP/NO-treated tumors, but the number of TUNEL-positive cells was not sufficient to inhibit tumor growth. Taken together, the Alb-PLP/NO NPs showed more potent anticancer effects than the other formulations. This occurred via enhanced induction of apoptosis caused by efficient NO delivery to a large number of cancer cells throughout the tumor tissue, a characteristic attributed to increased tumor penetration.

4. CONCLUSION

In this study, tumor-penetrable NO-releasing nanoparticles were developed for the local treatment of melanoma. Alb-PLP/NO NPs were successfully generated via three sequential processes: synthesis of PLP/NO, fabrication of the nanoparticles, and albumin coating on the surface of the positively charged PLP/NO NPs. The average particle size and ζ-potential of the Alb-PLP/NO NPs were 215.5 $\pm$ 3.2 nm and -8.5 ± 0.5 mV, and the nanoparticles could release 0.34 $\pm$ 0.03 μmol of NO/mg of particle in a sustained manner for more than 21 h. Owing to their prolonged NO release and enhanced cellular uptake, the Alb-PLP/NO NPs exhibited potent intracellular NO delivery and cytotoxicity in B16F10 cells compared with that of LP/NO treatment. *In vitro* ECM penetration and *in vivo* spatial distribution studies revealed that the spatial distribution in tumors was higher with Alb-PLP/NO NPs than with PLP/NO NPs, resulting from the enhanced ECM penetration caused by reduced electrostatic interactions between the nanoparticles and negatively charged ECM components. Finally, the Alb-PLP/NO NPs showed potent growth inhibitory effects on tumors without systemic toxicity

https://doi.org/10.1021/acsami.1c07407
ACS Appl. Mater. Interfaces 2021, 13, 30383−30396

in a murine melanoma mouse model through the efficient delivery of NO into melanoma cells throughout the entire tumor tissue because of enhanced tumor penetration. These results suggest that Alb-PLP/NO NPs are a promising formulation for the local treatment of melanoma.

■ ASSOCIATED CONTENT

Supporting Information

The Supporting Information is available free of charge at https://pubs.acs.org/doi/10.1021/acsami.1c07407.

Characterization of LP/NO (Figure S1); characterization of PLP/NO and ^{1}H NMR spectra of PLGA, LPEI, PLP, and PLP/NO (Figure S2); real-time NO release profiles of LP/NO and PLP/NO and cumulative NO release profiles of LP/NO-coated PLGA NPs and PLP/NO NPs (Figure S3); intracellular NO determination and cellular uptake of LPEI, LP/NO, PLP NPs, and PLP/NO NPs (Figure S4); CLSM images of intracellular NO determination (Figure S5); and representative IVIS images of the tumors treated with PLP NPs, PLP/NO NPs, Alb-PLP NPs, and Alb-PLP/NO NPs (Figure S6) (PDF)

■ AUTHOR INFORMATION

Corresponding Author

Jin-Wook Yoo − *College of Pharmacy, Pusan National University, Busan, South Korea;* orcid.org/0000-0001-5216-5518; Phone: +82-51-510-2807; Email: jinwook@pusan.ac.kr; Fax: +82 51 513 6754

Authors

Juho Lee − *College of Pharmacy, Pusan National University, Busan, South Korea*

Shwe Phyu Hlaing − *College of Pharmacy, Pusan National University, Busan, South Korea*

Nurhasni Hasan − *College of Pharmacy, Pusan National University, Busan, South Korea*

Dongmin Kwak − *College of Pharmacy, Pusan National University, Busan, South Korea*

Hyunwoo Kim − *College of Pharmacy, Pusan National University, Busan, South Korea*

Jiafu Cao − *State Key Laboratory for Functions and Applications of Medicinal Plants, Guizhou Medical University, Guiyang, China*

In-Soo Yoon − *College of Pharmacy, Pusan National University, Busan, South Korea*

Hwayoung Yun − *College of Pharmacy, Pusan National University, Busan, South Korea;* orcid.org/0000-0003-1414-6169

Yunjin Jung − *College of Pharmacy, Pusan National University, Busan, South Korea;* orcid.org/0000-0002-4794-483X

Complete contact information is available at: https://pubs.acs.org/10.1021/acsami.1c07407

Author Contributions

Conceptualization, J.L. and J-W.Y.; methodology, J.L., S.P.H., N.H., J.C., and D.K.; investigation, J.L., H.K., I.-S.Y., H.Y., J.C., and Y.J.; writing, J.L. and J-W.Y.; supervision, J-W.Y. All authors read and approved the final manuscript.

Funding

This research was supported by a Basic Science Research Program through the National Research Foundation of Korea (NRF) funded by the Ministry of Education (Grant No. 2019R1I1A3A01057849).

Notes

The authors declare no competing financial interest.

■ ABBREVIATIONS USED

NO; nitric oxide; ECM; extracellular matrix; PLGA; poly(D,L-lactic-*co*-glycolic acid); LP/NO; low molecular weight linear polyethylenimine diazeniumdiolate; PLP/NO; PLGA-conjugated LP/NO copolymer; BSA; bovine serum albumin; Alb-PLP/NO NPs; albumin-coated PLP/NO nanoparticles; LPEI; linear polyethylenimine; PVA; poly(vinyl alcohol); DAPI; 4′,6-diamidino-2-phenylindole dihydrochloride; MTT; thiazolyl blue tetrazolium bromide; NHS; *N*-hydroxysulfosuccinimide; EDC; 1-ethyl-3-(3-dimethylaminopropyl)carbodiimide hydrochloride; TUNEL; terminal deoxynucleotidyl transferase-deoxyuridine triphosphate nick end labeling; DAF-FM DA; 3-amino,4-aminomethyl-2′,7′-difluorescein diacetate; THF; tetrahydrofuran; DW; distilled water; DCM; dichloromethane; PBS; phosphate-buffered saline; O/W; oil-in-water; DMSO; dimethyl sulfoxide; CLSM; confocal laser scanning microscopy; PDI; polydispersity index; IVIS; *in vivo* imaging system; H&E; hematoxylin and eosin; EE; encapsulation efficiency; SGR; specific growth rate

■ REFERENCES

(1) Manier, K. K.; Maibach, H. I. *Skin Cancer Knowledge, Awareness, and Perception*; Springer International Publishing, 2021; pp 43−53.

(2) Dorrani, M.; Garbuzenko, O. B.; Minko, T.; Michniak-Kohn, B. Development of Edge-Activated Liposomes for siRNA Delivery to Human Basal Epidermis for Melanoma Therapy. *J. Controlled Release* **2016**, *228*, 150−158.

(3) Yang, S.; Liu, T.; Nan, H.; Wang, Y.; Chen, H.; Zhang, X.; Zhang, Y.; Shen, B.; Qian, P.; Xu, S.; et al. Comprehensive Analysis of Prognostic Immune-related Genes in the Tumor Microenvironment of Cutaneous Melanoma. *J. Cell. Physiol.* **2020**, *235* (2), 1025−1035.

(4) Paulson, K. G.; Gupta, D.; Kim, T. S.; Veatch, J. R.; Byrd, D. R.; Bhatia, S.; Wojcik, K.; Chapuis, A. G.; Thompson, J. A.; Madeleine, M. M.; et al. Age-Specific Incidence of Melanoma in the United States. *JAMA Dermatol.* **2020**, *156* (1), 57−64.

(5) Micali, G.; Lacarrubba, F.; Dinotta, F.; Massimino, D.; Nasca, M. R. Treating Skin Cancer with Topical Cream. *Expert Opin. Pharmacother.* **2010**, *11* (9), 1515−1527.

(6) Micali, G.; Lacarrubba, F.; Nasca, M. R.; Ferraro, S.; Schwartz, R. A. Topical Pharmacotherapy for Skin Cancer: Part II. Clinical Applications. *J. Am. Acad. Dermatol.* **2014**, *70* (6), 979.e1−979.e12.

(7) Navarrete-Dechent, C.; Nelson, K. C.; Rossi, A. M.; Lee, E. H.; Barker, C. A.; Nehal, K. S.; Swetter, S. M. *Lentigo Maligna Melanoma*; Springer, 2020; pp 925−951.

(8) Scarfì, F.; Patrizi, A.; Veronesi, G.; Lambertini, M.; Tartari, F.; Mussi, M.; Melotti, B.; Dika, E. The Role of Topical Imiquimod in Melanoma Cutaneous Metastases: A Critical Review of the Literature. *Dermatol. Ther.* **2020**, *33* (6), e14165.

(9) Winder, M.; Virós, A. Mechanisms of Drug Resistance in Melanoma. *Handb. Exp. Pharmacol.* **2017**, *249*, 91−108.

(10) Panizza, B. J.; de Souza, P.; Cooper, A.; Roohullah, A.; Karapetis, C. S.; Lickliter, J. D. Phase I Dose-Escalation Study to Determine the Safety, Tolerability, Preliminary Efficacy and Pharmacokinetics of an Intratumoral Injection of Tigilanol Tiglate (EBC-46). *EBioMedicine* **2019**, *50*, 433−441.

(11) Al-azzawi, S.; Masheta, D. Designing a Drug Delivery System for Improved Tumor Treatment and Targeting by Functionalization of a Cell-penetrating Peptide. *J. Pharm. Invest.* **2019**, *49* (6), 643−654.

(12) Vrouenraets, B. C.; Eggermont, A. M. M.; Hart, A. A. M.; Klaase, J. M.; Van Geel, A. N.; Nieweg, O. E.; Kroon, B. B. R. Regional Toxicity after Isolated Limb Perfusion with Melphalan and Tumour Necrosis Factor-α Versus Toxicity after Melphalan Alone. *European Journal of Surgical Oncology (EJSO)* **2001**, *27* (4), 390−395.
(13) Kroon, H. M.; Huismans, A. M.; Kam, P. C. A.; Thompson, J. F. Isolated Limb Infusion with Melphalan and Actinomycin D for Melanoma: a Systematic Review. *J. Surg. Oncol.* **2014**, *109* (4), 348−351.
(14) Kim, J.; Yung, B. C.; Kim, W. J.; Chen, X. Combination of Nitric Oxide and Drug Delivery Systems: Tools for Overcoming Drug Resistance in Chemotherapy. *J. Controlled Release* **2017**, *263*, 223−230.
(15) Carpenter, A. W.; Schoenfisch, M. H. Nitric Oxide Release: Part II. Therapeutic Applications. *Chem. Soc. Rev.* **2012**, *41* (10), 3742−3752.
(16) Kim, J.; Saravanakumar, G.; Choi, H. W.; Park, D.; Kim, W. J. A Platform for Nitric Oxide Delivery. *J. Mater. Chem. B* **2014**, *2* (4), 341−356.
(17) Huang, Z.; Fu, J.; Zhang, Y. Nitric Oxide Donor-based Cancer Therapy: Advances and Prospects. *J. Med. Chem.* **2017**, *60* (18), 7617−7635.
(18) Murphy, M. P. Nitric Oxide and Cell Death. *Biochim. Biophys. Acta, Bioenerg.* **1999**, *1411* (2−3), 401−414.
(19) Thomas, D. D.; Ridnour, L. A.; Isenberg, J. S.; Flores-Santana, W.; Switzer, C. H.; Donzelli, S.; Hussain, P.; Vecoli, C.; Paolocci, N.; Ambs, S.; et al. The Chemical Biology of Nitric Oxide: Implications in Cellular Signaling. *Free Radical Biol. Med.* **2008**, *45* (1), 18−31.
(20) Thomas, D. D.; Espey, M. G.; Ridnour, L. A.; Hofseth, L. J.; Mancardi, D.; Harris, C. C.; Wink, D. A. Hypoxic Inducible Factor 1α, Extracellular Signal-Regulated Kinase, and p53 are Regulated by Distinct Threshold Concentrations of Nitric Oxide. *Proc. Natl. Acad. Sci. U. S. A.* **2004**, *101* (24), 8894−8899.
(21) Forrester, K.; Ambs, S.; Lupold, S. E.; Kapust, R. B.; Spillare, E. A.; Weinberg, W. C.; Felley-Bosco, E.; Wang, X. W.; Geller, D. A.; Tzeng, E.; et al. Nitric Oxide-induced p53 Accumulation and Regulation of Inducible Nitric Oxide Synthase Expression by Wild-Type p53. *Proc. Natl. Acad. Sci. U. S. A.* **1996**, *93* (6), 2442−2447.
(22) Glockzin, S.; von Knethen, A.; Scheffner, M.; Brüne, B. Activation of the Cell Death Program by Nitric Oxide Involves Inhibition of the Proteasome. *J. Biol. Chem.* **1999**, *274* (28), 19581−19586.
(23) Boyd, C. S.; Cadenas, E. Nitric Oxide and Cell Signaling Pathways in Mitochondrial-Dependent Apoptosis. *Biol. Chem.* **2002**, *383* (3−4), 411−423.
(24) Schaer, D. A.; Hirschhorn-Cymerman, D.; Wolchok, J. D. Targeting Tumor-Necrosis Factor Receptor Pathways for Tumor Immunotherapy. *Journal for immunotherapy of cancer* **2014**, *2* (1), 7.
(25) Lala, P. K.; Chakraborty, C. Role of Nitric Oxide in Carcinogenesis and Tumour Progression. *Lancet Oncol.* **2001**, *2* (3), 149−156.
(26) Lee, J.; Hlaing, S. P.; Cao, J.; Hasan, N.; Yoo, J.-W. In Vitro and in Vivo Evaluation of a Novel Nitric Oxide-Releasing Ointment for the Treatment of Methicillin-Resistant Staphylococcus Aureus-infected Wounds. *J. Pharm. Investig.* **2020**, *50* (5), 505−512.
(27) Lee, H. J.; Park, D. J.; Choi, G. H.; Yang, D.-N.; Heo, J. S.; Kim, D. E.; Lee, S. C. pH-Responsive Mineralized Nanoparticles as Stable Nanocarriers for Intracellular Nitric Oxide Delivery. *Colloids Surf., B* **2016**, *146*, 1−8.
(28) Lee, S. Y.; Rim, Y.; McPherson, D. D.; Huang, S.-L.; Kim, H. A Novel Liposomal Nanomedicine for Nitric Oxide Delivery and Breast Cancer Treatment. *Bio-Med. Mater. Eng.* **2014**, *24* (1), 61−67.
(29) Seabra, A.; Lima, R.; Calderon, M. Nitric Oxide Releasing Nanomaterials for Cancer Treatment: Current Status and Perspectives. *Curr. Top. Medi. Chem.* **2015**, *15* (4), 298−308.
(30) Stevens, E. V.; Carpenter, A. W.; Shin, J. H.; Liu, J.; Der, C. J.; Schoenfisch, M. H. Nitric Oxide-Releasing Silica Nanoparticle Inhibition of Ovarian Cancer Cell Growth. *Mol. Pharmaceutics* **2010**, *7* (3), 775−785.
(31) Pelegrino, M. T.; Silva, L. C.; Watashi, C. M.; Haddad, P. S.; Rodrigues, T.; Seabra, A. B. Nitric Oxide-Releasing Nanoparticles: Synthesis, Characterization, and Cytotoxicity to Tumorigenic Cells. *J. Nanopart. Res.* **2017**, *19* (2), 57.
(32) Fong, E. L. S.; Harrington, D. A.; Farach-Carson, M. C.; Yu, H. Heralding a New Paradigm in 3D Tumor Modeling. *Biomaterials* **2016**, *108*, 197−213.
(33) Parodi, A.; Haddix, S. G.; Taghipour, N.; Scaria, S.; Taraballi, F.; Cevenini, A.; Yazdi, I. K.; Corbo, C.; Palomba, R.; Khaled, S. Z.; et al. Bromelain Surface Modification Increases the Diffusion of Silica Nanoparticles in the Tumor Extracellular Matrix. *ACS Nano* **2014**, *8* (10), 9874−9883.
(34) Henke, E.; Nandigama, R.; Ergün, S. Extracellular Matrix in the Tumor Microenvironment and Its Impact on Cancer Therapy. *Frontiers in molecular biosciences* **2020**, *6*, 160.
(35) Barone, M.; Sciortino, M. T.; Zaccaria, D.; Mazzaglia, A.; Sortino, S. Nitric Oxide Photocaging Platinum Nanoparticles with Anticancer Potential. *J. Mater. Chem.* **2008**, *18* (45), 5531−5536.
(36) Sonveaux, P.; Jordan, B. F.; Gallez, B.; Feron, O. Nitric Oxide Delivery to Cancer: Why and How? *Eur. J. Cancer* **2009**, *45* (8), 1352−69.
(37) Seabra, A. B.; Durán, N. Nitric Oxide-Releasing Vehicles for Biomedical Applications. *J. Mater. Chem.* **2010**, *20* (9), 1624−1637.
(38) Bauer, J. A.; Rao, W.; Smith, D. J. Evaluation of Linear Polyethyleneimine/Nitric Oxide Adduct on Wound Repair: Therapy Versus Toxicity. *Wound Repair and Regeneration* **1998**, *6* (6), 569−577.
(39) Mowery, K. A.; Schoenfisch, M. H.; Saavedra, J. E.; Keefer, L. K.; Meyerhoff, M. E. Preparation and Characterization of Hydrophobic Polymeric Films That Are Thromboresistant Via Nitric Oxide Release. *Biomaterials* **2000**, *21* (1), 9−21.
(40) Cha, K. H.; Wang, X.; Meyerhoff, M. E. Nitric Oxide Release for Improving Performance of Implantable Chemical Sensors−A Review. *Applied materials today* **2017**, *9*, 589−597.
(41) Brisbois, E. J.; Handa, H.; Meyerhoff, M. E. *Advanced Polymers in Medicine*; Springer, 2015; pp 481−511.
(42) Gofrit, O. N.; Benjamin, S.; Halachmi, S.; Leibovitch, I.; Dotan, Z.; Lamm, D. L.; Ehrlich, N.; Yutkin, V.; Ben-Am, M.; Hochberg, A. DNA Based Therapy with Diphtheria Toxin-A BC-819: a Phase 2b Marker Lesion Trial in Patients with Intermediate Risk Nonmuscle Invasive Bladder Cancer. *J. Urol.* **2014**, *191* (6), 1697−1702.
(43) Halachmi, S.; Leibovitch, I.; Zisman, A.; Stein, A.; Benjamin, S.; Sidi, A.; Knickerbocker, R.; Limor, M.; Moore, Y. Phase II Trial of BC-819 Intravesical Gene Therapy in Combination with BCG in Patients with Non-Muscle Invasive Bladder Cancer (NMIBC). *J. Clin. Oncol.* **2018**, *36*, 499.
(44) Patnaik, S.; Gupta, K. C. Novel Polyethylenimine-Derived Nanoparticles for In Vivo Gene Delivery. *Expert Opin. Drug Delivery* **2013**, *10* (2), 215−228.
(45) Stylianopoulos, T.; Poh, M.-Z.; Insin, N.; Bawendi, M. G.; Fukumura, D.; Munn, L. L.; Jain, R. K. Diffusion of Particles in the Extracellular Matrix: the Effect of Repulsive Electrostatic Interactions. *Biophys. J.* **2010**, *99* (5), 1342−1349.
(46) Hyun, H.; Park, J.; Willis, K.; Park, J. E.; Lyle, L. T.; Lee, W.; Yeo, Y. Surface Modification of Polymer Nanoparticles with Native Albumin for Enhancing Drug Delivery to Solid Tumors. *Biomaterials* **2018**, *180*, 206−224.
(47) Jiang, Y.; Lu, H.; Dag, A.; Hart-Smith, G.; Stenzel, M. H. Albumin−Polymer Conjugate Nanoparticles and Their Interactions with Prostate Cancer Cells in 2D and 3D Culture: Comparison Between PMMA and PCL. *J. Mater. Chem. B* **2016**, *4* (11), 2017−2027.
(48) Commisso, C.; Davidson, S. M.; Soydaner-Azeloglu, R. G.; Parker, S. J.; Kamphorst, J. J.; Hackett, S.; Grabocka, E.; Nofal, M.; Drebin, J. A.; Thompson, C. B.; et al. Macropinocytosis of Protein is an Amino Acid Supply Route in Ras-Transformed Cells. *Nature* **2013**, *497* (7451), 633−637.
(49) Kim, J.; Lee, Y.; Singha, K.; Kim, H. W.; Shin, J. H.; Jo, S.; Han, D.-K.; Kim, W. J. NONOates−Polyethylenimine Hydrogel for

https://doi.org/10.1021/acsami.1c07407
ACS Appl. Mater. Interfaces 2021, 13, 30383−30396

Controlled Nitric Oxide Release and Cell Proliferation Modulation. *Bioconjugate Chem.* **2011**, *22* (6), 1031−1038.
(50) Lee, J.; Kwak, D.; Kim, H.; Kim, J.; Hlaing, S. P.; Hasan, N.; Cao, J.; Yoo, J.-W. Nitric Oxide-Releasing S-Nitrosoglutathione-Conjugated Poly (Lactic-Co-Glycolic Acid) Nanoparticles for the Treatment of MRSA-Infected Cutaneous Wounds. *Pharmaceutics* **2020**, *12* (7), 618.
(51) Hetrick, E. M.; Shin, J. H.; Paul, H. S.; Schoenfisch, M. H. Anti-Biofilm Efficacy of Nitric Oxide-Releasing Silica Nanoparticles. *Biomaterials* **2009**, *30* (14), 2782−2789.
(52) Laurent, C. D. S.; Moon, T. C.; Befus, A. D. Measurement of Nitric Oxide in Mast Cells with the Fluorescent Indicator DAF-FM Diacetate. *Mast Cells*; Springer, 2015; pp 339−345.
(53) Patil, S. C.; Tagalpallewar, A. A.; Kokare, C. R. Natural Anti-Proliferative Agent Loaded Self-Microemulsifying Nanoparticles for Potential Therapy in Oral Squamous Carcinoma. *J. Pharm. Invest.* **2019**, *49* (5), 527−541.
(54) Park, J.; Sun, B.; Yeo, Y. Albumin-Coated Nanocrystals for Carrier-Free Delivery of Paclitaxel. *J. Controlled Release* **2017**, *263*, 90−101.
(55) Mehrara, E.; Forssell-Aronsson, E.; Ahlman, H.; Bernhardt, P. Specific Growth Rate Versus Doubling Time for Quantitative Characterization of Tumor Growth Rate. *Cancer Res.* **2007**, *67* (8), 3970−3975.
(56) Stamler, J. S.; Jaraki, O.; Osborne, J.; Simon, D. I.; Keaney, J.; Vita, J.; Singel, D.; Valeri, C. R.; Loscalzo, J. Nitric Oxide Circulates in Mammalian Plasma Primarily as an S-nitroso Adduct of Serum Albumin. *Proc. Natl. Acad. Sci. U. S. A.* **1992**, *89* (16), 7674.
(57) Dempsey, C.; Lee, I.; Cowan, K. R.; Suh, J. Coating Barium Titanate Nanoparticles with Polyethylenimine Improves Cellular Uptake and Allows for Coupled Imaging and Gene Delivery. *Colloids Surf., B* **2013**, *112*, 108−112.
(58) Park, J. E.; Park, J.; Jun, Y.; Oh, Y.; Ryoo, G.; Jeong, Y.-S.; Gadalla, H. H.; Min, J. S.; Jo, J. H.; Song, M. G.; et al. Expanding Therapeutic Utility of Carfilzomib for Breast Cancer Therapy by Novel Albumin-Coated Nanocrystal Formulation. *J. Controlled Release* **2019**, *302*, 148−159.
(59) Kudarha, R. R.; Sawant, K. K. Albumin Based Versatile Multifunctional Nanocarriers for Cancer Therapy: Fabrication, Surface Modification, Multimodal Therapeutics and Imaging Approaches. *Mater. Sci. Eng., C* **2017**, *81*, 607−626.
(60) Da Rocha, E.; Porto, L.; Rambo, C. Nanotechnology Meets 3D in Vitro Models: Tissue Engineered Tumors and Cancer Therapies. *Mater. Sci. Eng., C* **2014**, *34*, 270−279.
(61) Lieleg, O.; Baumgärtel, R. M.; Bausch, A. R. Selective Filtering of Particles by the Extracellular Matrix: an Electrostatic Bandpass. *Biophys. J.* **2009**, *97* (6), 1569−1577.

https://doi.org/10.1021/acsami.1c07407
ACS Appl. Mater. Interfaces 2021, 13, 30383−30396